ELSEVIER

Marangoni-driven liquid films rising out of a meniscus onto a nearly-horizontal substrate

Andreas Münch[a,b,*], P.L. Evans[a]

[a] *Humboldt University of Berlin, Institute of Mathematics, 10099 Berlin, Germany*
[b] *Weierstrass Institute for Applied Analysis and Stochastics (WIAS), Mohrenstraße 39, 10117 Berlin, Germany*

Abstract

We revisit the situation of a thin liquid film driven up an inclined substrate by a thermally induced Marangoni shear stress against the opposing parallel component of gravity. In contrast to previous studies, we focus here on the meniscus region, in a case where the substrate is nearly horizontal. Our numerical simulations show that the time-dependent lubrication model for the film profile can reach a steady state in the meniscus region that is unlike the monotonic solutions found in [A. Münch, The thickness of a Marangoni-driven thin liquid film emerging from a meniscus, SIAM J. Appl. Math. 62 (6) (2002) 2045–2063]. A systematic investigation of the steady states of the lubrication model is carried out by studying the phase space of the corresponding third-order ODE system. We find a rich structure of the phase space including multiple non-monotonic solutions with the same far-field film thickness.
© 2005 Elsevier B.V. All rights reserved.

1. Introduction

In recent years, various aspects of the formation and behavior of thin liquid films that climb out of a reservoir along an inclined wafer under the action of a thermally induced Marangoni shear stress have been intensively investigated, e.g., [1–6]. The basic setup, introduced in the first reference, is shown in Fig. 1. A silicon wafer, tilted at an angle α from the vertical

position, is subject to a temperature gradient between two heaters that maintain a temperature of T_+ at its lower end, and of $T_- < T_+$ at its upper end. The lower end of the wafer is submerged in a reservoir of silicon oil. At the beginning of the experiment, the level of the liquid in the reservoir is kept below the region where the temperature gradient sets in. The fluid therefore achieves a thermal and hydrostatic equilibrium, with a meniscus that extends a certain distance up the wafer.

Then the liquid of the reservoir is raised by slowly adding liquid from an external supply (not shown in the figure), until the meniscus just reaches into the

---

* Corresponding author.
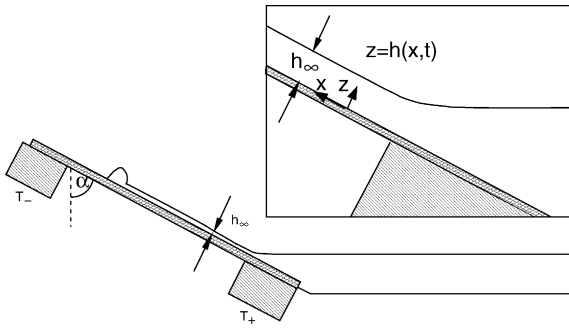 *E-mail address:* muench@mathematik.hu-berlin.de (A. Münch).

Fig. 1. Sketch of the experimental setup with the wafer in a close to horizontal position (i.e., at a large inclination angle α with respect to the vertical position). The substrate is subject to a temperature gradient between the heaters that are held at temperatures $T_+ > T_-$. This induces a Marangoni shear stress that moves a thin liquid film up the wafer.

thermal gradient region. As a result, the liquid in the upper part of the meniscus experiences a thermal gradient, which leads to a gradient in the temperature dependent surface tension coefficient, so that the surface tension increases with distance above the reservoir. Consequently, a Marangoni shear stress sets in at the liquid/air interface, which pulls a thin film of liquid out of the reservoir, up along the wafer.

Once the contact line has moved sufficiently far from the reservoir's surface, the film profile becomes stationary near the meniscus. For some distance above the meniscus, the film has a nearly uniform thickness h_∞. Towards the rising contact line, the film can evolve into either a single traveling wave or a double wave structure [6,7]. In the latter case, the leading part of the double wave is a nonclassical undercompressive wave. Further work extended these results on the wave dynamics in a number of directions [8,9]. It has been found that the film thickness h_∞ plays an important role in determining the outcome, i.e., which of the different wave structures evolve. Various aspects of the film profiles in the contact line region, including their stability, have also been studied in [4,5].

The film thickness h_∞ has usually been treated as an independent parameter in the aforementioned theoretical investigations, but for the experimental setup discussed here and in most of the above references, h_∞ is typically determined by the meniscus. This phenomenon is related to the Landau–Levich drag-out problem of determining the thickness of an isothermal

liquid film deposited onto a substrate that is pulled out of a liquid reservoir. Using ideas from matched asymptotics, Landau and Levich [10] were able to understand how the meniscus that forms where the substrate leaves the reservoir controls the thickness h_∞. They provided a leading order result for the thickness as a function of the liquid properties and the withdrawal speed, for the case of a vertical substrate.

Landau and Levich's ideas were extended to the Marangoni-driven film and non-zero inclination angles by Carles and Cazabat [2]. A subsequent study [3] revealed a systematic deviation of theory and experimental thickness measurements of up to about 20%. This discrepancy is connected to the presence of logarithmic terms in the next order corrections [11,12]. Münch [12] provides a derivation of the complete correction term for non-zero inclination angles via a systematic application of matched asymptotics. These results, however, did not extend to substrates that are tilted close to a horizontal position.

In this paper, we focus on the situation of nearly horizontal wafers, that is, inclination angles α that satisfy $\cot\alpha \ll 1$, by first performing numerical simulations of the time-dependent lubrication model for the two-dimensional flow, and then investigating the phase space of the third-order ODE that describes a stationary meniscus. Our study reveals a number of new meniscus solutions which do not select the thickness h_∞ ahead of the meniscus.

These findings are related to similar results for coating films on a stationary or moving substrate obtained by a number of authors following Landau and Levich's work. Wilson [13] investigated the drag-out problem for general inclination angles, and determined the film thickness by solving, via matched asymptotics, a boundary value problem for the free surface. He noticed a non-uniformity in his solution as α approached $\pi/2$, and observed that the meniscus solution ceased to exist if $\pi/2 - \alpha$ was smaller than a critical value (depending on the withdrawal speed). Furthermore, Wilson observed that these solutions were not always unique. The latter issue was taken up again by Hocking [14], who recognized the importance of the contact-line region in determining the film thickness for a range of withdrawal speeds. Kheshgi et al. [15] also discussed the steady state problem for the meniscus region and identified two types of solutions, one that fixes the flow rate according to the wall velocity and

reservoir configuration, and a second type where the flow rate can be chosen independently. However, none of these authors systematically investigated the three-dimensional phase space of the steady state ODEs.

The paper is organized as follows: in Section 2, we formulate the dimensional model for the meniscus/film driven by Marangoni shear stresses and give scalings that lead to a lubrication model that is valid in the entire film including the meniscus. Section 3 presents results of numerical simulations showing different examples of how a meniscus can evolve starting from monotonic initial data. Stationary solutions satisfying the meniscus far-field conditions are considered in Section 4 via investigation of the three-dimensional phase space of the corresponding third-order ODE. In Section 5, we summarize and discuss our results.

2. Formulation

In [12], a stationary model was derived for the meniscus profile using ideas from singular perturbation theory to reduce the free boundary problem for the coupled Stokes and energy equations to a boundary value problem for a scalar third-order ODE for the case $\alpha > 0$. The corresponding boundary value problem for a vertical wafer position was given in [11] and the time-dependent fourth order PDE was used in [16] to investigate the pinch-off instability in an experiment by Ludviksson and Lightfoot [17]. Generalizing these approaches, the evolution of the dimensionless film/meniscus profile $z = h(x, t)$ is governed by

$$h_t + \Omega_x(h^2)_x - (h^3)_x = -(h^3\kappa_x)_x + D(h^3 h_x)_x, \quad (1)$$

where

$$\kappa = \frac{h_{xx}}{(1 + \epsilon^2 h_x^2)^{3/2}}$$

is the nonlinear expression for curvature. The quadratic and cubic terms on the left side of (1) represent the contribution of the Marangoni shear stress (where the prefactor Ω_x represents the spatial derivative of a temperature profile, explained further below) and the counteracting component of gravity parallel to the wafer. On the right hand side, the first term arises from surface tension and the second from the contribution of the normal component of gravity.

The above equation was non-dimensionalized using the following scalings for x, z and t, respectively,

$$L = \left(\frac{3\sigma\gamma\sigma_T}{2\rho^2 g^2 \cos^2\alpha}\right)^{1/3}, \quad H = \frac{3\gamma\sigma_T}{2\rho g \cos\alpha},$$

$$\tau = \frac{2^{5/3}\mu\,(\sigma\rho g \cos\alpha)^{1/3}}{3^{2/3}(\gamma\sigma_T)^{5/3}}, \quad (2)$$

and contains two dimensionless parameters, the length scale ratio ϵ and the parameter D, which measures the relative importance of the normal component of gravity. These are defined by

$$\epsilon = \frac{H}{L} = \left(\frac{9}{4}\frac{\gamma^2\sigma_T^2}{\sigma\rho g \cos\alpha}\right)^{1/3} \quad \text{and} \quad D = \frac{\epsilon}{\cot\alpha}. \quad (3)$$

The dimensional quantities that appear here are the mean surface tension of the liquid/air interface σ, the temperature gradient γ, the dependence of surface tension on temperature $\sigma_T = d\sigma/dT$, the liquid viscosity μ, the density ρ, and the gravitational acceleration g. We note that ϵ can be connected to a capillary number $\text{Ca} = \mu(L/\tau)/\sigma$ via $\epsilon = (3\text{Ca})^{1/3}$.

Previous work by Münch [12] introduced a temperature profile $\Omega = \Omega(x)$ that cuts off surface tension gradients in the meniscus region near the lower heater. The rationale for this choice is the actual experimental setting where the temperature gradient, hence the surface tension gradient, is constant along the substrate and the film except near the heaters, where it drops to zero. The cut-off was set at a position, say $x = x_c$, below the rising height for an isothermal, static meniscus on a perfectly wetting substrate.

Eq. (1) requires boundary conditions. Far above the meniscus, we use a precursor model to alleviate the well-known singularity near a moving contact line,

$$h(x, t) \rightarrow b \quad \text{for} \quad x \rightarrow \infty. \quad (4)$$

In the other direction, the meniscus flattens out onto the surface of the undisturbed reservoir,

$$h(x, t) \sim -\frac{x}{D} \quad \text{for} \quad x \rightarrow -\infty. \quad (5)$$

In this paper, we consider a specific limiting problem for (1), (4), (5), namely, $\epsilon \ll 1$ with $\epsilon \ll D$ where D is order one or smaller, and a further condition on the heating profile that we discuss below. The first condition ensures that the length scale ratio H/L in the

thin film region allows use of the lubrication approximation. The second, $\epsilon \ll D$, implies that $\epsilon|h_x| \ll 1$ even in the vicinity of the reservoir, where the slope h_x is determined by (5). The relation $\epsilon|h_x| \ll 1$ permits us to replace the κ in (1) by the linearized curvature, i.e., lubrication theory holds throughout the film and the meniscus including the reservoir. The remaining condition on D is required to ensure that the fourth order term from surface tension enters the dominant balance in (1), and is not outperformed by the second-order term arising from the normal component of gravity.

We now give an interpretation of these conditions in terms of the elevation angle $\hat{\alpha} = \pi/2 - \alpha$ with respect to the horizontal position and the parameter $\delta = \gamma\sigma_T/(4\sigma\rho g)^{1/2}$. This parameter played the role of the lubrication parameter in the scalings used for example in [16]. It can be thought of as a non-dimensional measure of the shear stress and is indeed small in typical physical experiments [1,2,18,19]. Using

$$\epsilon = \left(\frac{9\delta^2}{\sin\hat{\alpha}}\right)^{1/3}, \quad D = \left(\frac{3\delta}{\sin^2\hat{\alpha}}\right)^{2/3}\cos\hat{\alpha},$$

one easily finds that $\epsilon \ll D \ll 1$ and $\epsilon \ll D \sim 1$ are equivalent to $\delta \ll \hat{\alpha}^2 \ll 1$ and $\delta \sim \hat{\alpha}^2 \ll 1$, respectively. Hence the limits we have specified above correspond to a certain regime of small shear stress and nearly-horizontal wafer positions.

With the above conditions satisfied, (1) becomes

$$h_t + [f(h)]_x = -(h^3 h_{xxx})_x + D(h^3 h_x)_x, \quad (6)$$

where $f(h) = h^2 - h^3$ denotes the flux-function. Note that in (6), we let $\Omega_x \to 1$. This additional condition requires that as the substrate is lowered ($\hat{\alpha} \to 0$), the position of the heater is moved further into the bath so that in the limit, the liquid film is subject to a uniform shear stress. In the following section, we discuss (6) with far-field conditions (4) and (5) for $D > 0$.

3. Dynamical simulation

We seek solutions for the PDE (6) using initial data which satisfies the far-field conditions (4) and (5). Specifically, the initial profile for our computations consists of a static meniscus smoothly joined to the precursor film. The static meniscus arises in the absence of Marangoni forces through the balance of mean surface tension and gravity. Its profile is governed by the ODE $h_{xxx} = Dh_x + 1$ and the boundary conditions $h \sim -x/D$ for $x \to -\infty$ and $h(0) = 0 = h_x(0)$. The conditions at $x = 0$ ensure that the 'tip' of the meniscus is located at the origin and levels out onto the substrate with zero contact angle. Raising this profile by an amount b permits it to be smoothly joined to a precursor film starting at $x = 0$. Thus, the initial profile is:

$$h_0(x) = \begin{cases} D^{-3/2}(\exp(D^{1/2}x) \\ \quad -D^{1/2}x - 1) + b & \text{for} \quad x \le 0, \quad (7) \\ b & \text{for} \quad x > 0. \end{cases}$$

To obtain solutions of (6) numerically, we truncate the infinite spatial domain to $[x_1, x_2] = [-l/5, 4l/5]$, with the length of the domain chosen to be about $l = 100$. We impose four boundary conditions, requiring $h_x(x_2, t) = 0$, $h_{xxx}(x_2, t) = 0$ and $h(x_1, t) = h_0(x_1)$, $h_{xxx}(x_1, t) = 0$ for $t > 0$. We discretize the initial boundary value problem on this domain using standard finite differences in space and an implicit Euler scheme in time. Grid points are concentrated near where the evolving wave structure joins the precursor. After each time step, the solution is transferred via interpolation onto a new grid shifted to match the new position of the leading front. The time discretization error is controlled using a step-doubling approach. All calculations are carried out in quadruple precision arithmetic in order to obtain accurate results for fourth order PDEs discretized on a fine grid [20].

In the following, we consider three examples, using a fixed value of $b = 0.005$ for the precursor film thickness with three different values for $D = 0.1021, 0.3220$, and 0.6426. For a fixed temperature gradient, increasing the parameter D corresponds to lowering the wafer to more horizontal positions in a physical experiment.

Example 1. $D = 0.1021$.

At first, a rapidly growing ridge forms at the meniscus. The ridge then separates off and begins to rise up the wafer. For the smallest choice of D, the shape of the ridge saturates, forming a single compressive wave, traveling with constant speed in the positive x
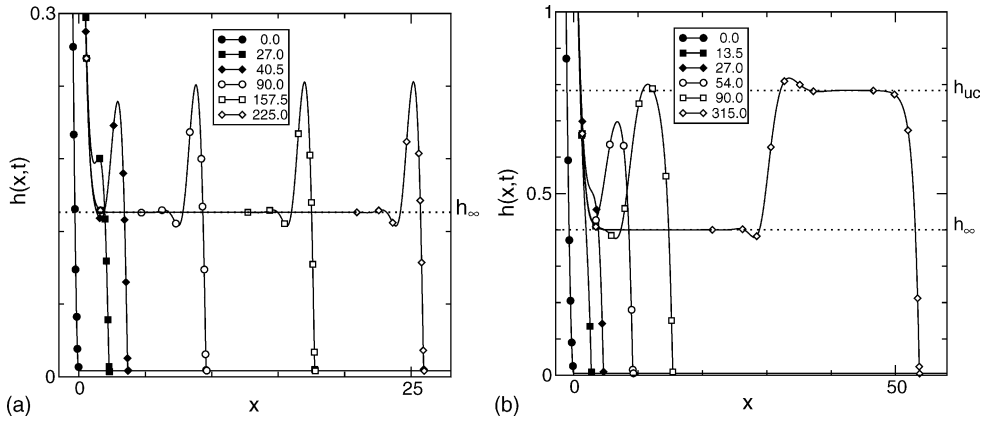
Fig. 2. Numerical solutions of (6) and (7) for Example 1 ((a), left) and Example 2 ((b), right). Film profiles are shown at dimensionless times as given in the legends. In (a), there is a single compressive wave, while in (b), an undercompressive-Lax double shock develops and travels up the substrate. There is a thin precursor film of thickness $b = 0.005$ in both cases.

direction (see Fig. 2(a)). A compressive (or Lax) wave [7] is one for which the characteristic speeds for the left and right state h_∞ and b satisfy the so-called Lax entropy condition $f'(h_\infty) < s(h_\infty, b) < f'(b)$, where the wave speed s is given by the Rankine-Hugoniot condition $s = (f(h_\infty) - f(b))/(h_\infty - b)$. As it moves further away, the meniscus settles into a monotonic, stationary solution with h_∞ as far-field thickness for large positive x. The value of h_∞ depends on D but is not affected if we perturb the value of b.

Example 2. $D = 0.3220$.

For this somewhat larger value of D, the shape of the capillary ridge does not saturate, in contrast to the previous example. We see in Fig. 2(b) that a ridge forms as before, but begins to pull apart to form the typical profile of a double wave with two separating fronts. The leading wave is a nonclassical undercompressive wave with a unique, b- and D-dependent left state h_{uc} for which the Lax condition is violated (i.e., $f'(h_{uc}) < s(h_{uc}, b)$), while the trailing wave is a classical compressive or Lax wave; a detailed investigation of the double wave can be found in [6–8]. The compressive wave moves at a lower speed than the undercompressive wave, but both speeds are positive, so that for long times, the meniscus evolves into a stationary monotonic solution with far-field film thickness h_∞ which depends on D but not on b, as in the first example.

Example 3. $D = 0.6426$.

For the largest value of D we consider in this section, the development in the beginning is similar to the second example: we see the formation of an undercompressive wave (Fig. 3), that moves up the wafer. In its wake, a structure with a visible dip emerges, which, however, remains attached to the meniscus, i.e., it persists even for long times as the undercompressive wave moves further up the wafer. The meniscus evolves into a stationary profile that is non-monotonic, with $h_\infty = h_{uc}$. In this example, the far-field thickness is set by the undercompressive wave, so it depends on b in addition to D.

4. Steady state solutions

4.1. Steady state equations

We next explicitly seek steady state solutions of Eq. (6). Setting $h_t = 0$ and integrating once yields a third-order ODE for h,

$$h_{xxx} - Dh_x = -\frac{f(h) - Q}{h^3}, \tag{8}$$

where the constant of integration Q represents the total flux of liquid across a cross-section of the film. Specifically, we look for solutions that extend from the reservoir at $x \to -\infty$ onto a flat film at $x \to \infty$, i.e., that
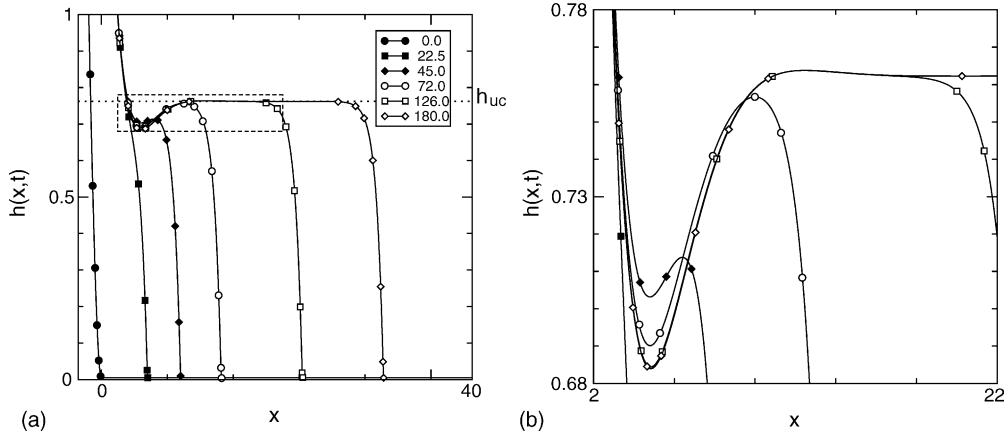
Fig. 3. Numerical solution of (6) and (7) for Example 3, at dimensionless times given in the legends. Only the undercompressive shock propagates away from the meniscus. The right figure (b) shows an enlarged view of the region in the left figure (a) delineated by a dashed box. Again the precursor layer thickness is $b = 0.005$.

satisfy the far-field conditions

$$h(x, t) \sim h_\infty \quad \text{for} \quad x \to \infty, \tag{9}$$

$$h(x, t) \sim -\frac{x}{D} \quad \text{for} \quad x \to -\infty. \tag{10}$$

From (8) and (9), we readily find that Q and h_∞ are related via the flux function, $Q = f(h_\infty)$. For given Q in the range $0 \leq Q < f(2/3) = 4/27$, there are exactly two positive solutions h_∞ that satisfy this relation. The lower solution, h_B, lies in the range $0 < h_B < 2/3$ and increases with Q, while the upper, h_T, satisfies $2/3 < h_T < 1$ and decreases. For $Q \to 0$, h_B and h_T tend to 0 and 1, respectively, and for $Q \to 4/27$, they merge at $h = 2/3$.

In the following, we identify the solutions of (8)–(10) with h_∞ equal to either h_B or h_T, by investigating the three-dimensional phase space of (8). There are two parameters in (8), D and Q. However, rather than using Q itself as second parameter, we use the corresponding lower film thickness h_B, $0 < h_B < 2/3$. From h_B we can determine the total flux $Q = f(h_B)$, and the upper thickness h_T, $2/3 < h_T < 1$, by solving $f(h_T) = Q$. As is made clear below, the solutions of (8)–(10) with far-field thickness $h_\infty = h_B$ are qualitatively distinct from those where $h_\infty = h_T$. We will subsequently refer to the former as Type I and to the latter as Type II meniscus solutions.

Letting $v = h'$ and $w = h''$, we convert (8) into a system of three first order ODEs

$$h' = v, \quad v' = w, \quad w' = Dv - \frac{f(h) - f(h_B)}{h^3}, \tag{11}$$

where primes denote derivatives with respect to x.

4.2. Equilibria and invariant manifolds

The system (11) has two equilibria, the 'bottom' equilibrium $B = (h_B, 0, 0)$ and the 'top' equilibrium $T = (h_T, 0, 0)$. Linearizing (11) near an equilibrium $I \in \{B, T\}$, we find the characteristic equation for the eigenvalues of the linearized ODE system to be

$$\lambda^3 - D\lambda + \frac{f'(h_I)}{h_I^3} = 0. \tag{12}$$

For both choices of $I \in \{B, T\}$, the roots of this polynomial equation have non-zero real part since $f'(h_I)$ is non-zero. Moreover, the sum of the three roots of (12) must be zero, so there must be real roots or real parts of complex conjugate roots of both signs, hence B and T are saddle points. The equilibrium coating thicknesses h_B and h_T are functions of D; in what follows we will only on occasion note this dependence explicitly.

For the bottom fixed point, we have $f'(h_B) > 0$, so that the product of the eigenvalues must be negative.

This implies that exactly one eigenvalue is real and negative; the other two are either real and positive or form a complex conjugate pair with positive real part. The distinction between these two cases is provided by the sign of the discriminant

$$\Delta(h; D) = -\frac{D^3}{27} + \frac{(f'(h)/h^3)^2}{4}. \tag{13}$$

If $\Delta(h_B; D) > 0$, we have a complex conjugate pair, while for $\Delta(h_B; D) \leq 0$, all roots are real. Hence B has a one-dimensional stable manifold $W^s(B)$ and a two-dimensional unstable one, $W^u(B)$. Trajectories on the latter form a spiral near B in the case where we have a complex conjugate pair of eigenvalues, i.e., if $\Delta(h_B; D)$ is positive.

For the top fixed point, $f'(h_T) < 0$, so it has a one-dimensional unstable manifold $W^u(T)$ and a two-dimensional stable manifold $W^s(T)$. The eigenvalue corresponding to $W^u(T)$ is real while the eigenvalues for $W^s(T)$ are complex conjugate exactly if $\Delta(h_T; D) > 0$; in that case, the trajectories on $W^s(T)$ wind into a spiral near T. For $\Delta(h_T; D) \leq 0$, all eigenvalues are real.

We now turn to characterizing the trajectories that have the proper behavior for $x \to -\infty$, i.e., that satisfy (10). Expanding h in terms of x yields a special solution, $h_0(x)$, the first terms of which are

$$h_0(x) = -\frac{x}{D} - \ln |x| + o(1) \quad \text{at} \quad x \to -\infty. \tag{14}$$

The behavior of the general solution of (8) at $x \to -\infty$ that satisfies (10) is given by

$$h(x) \sim h_0(x) + C_0 + C_1 \exp(D^{1/2}x) \quad \text{at} \quad x \to -\infty. \tag{15}$$

Here, C_0 and C_1 are arbitrary constants. The first of these two constants, C_0, corresponds to translations of the solution along the x-axis; since solutions to (8)–(10) are translation invariant, we can set $C_0 = 0$ without loss of generality. From this, we conclude that the solutions of (8) that satisfy (10) form a one parameter family, which corresponds to a two-dimensional manifold W^∞ in the phase space for (11). We note that solutions satisfying the far field condition (10) can be represented as trajectories approaching an equilibrium, by writing (8) as a new system of ODEs with independent variables $\tilde{u} = 1/h$, $\tilde{v} = h_x$ and $\tilde{w} = h_{xx}$. Then

these solutions become trajectories of the new system that tend to the equilibrium $(\tilde{u}, \tilde{v}, \tilde{w}) = (0, -1/D, 0)$. In this paper, however, we continue with the system (11) that represents meniscus profiles directly.

Type I meniscus solutions arise as codimension one intersections of W^∞ and $W^s(B)$ and therefore break under perturbations of h_B for fixed D. This agrees with previous findings [12] for a model with nonlinear curvature and small α, that matching inner and outer solutions for Type I meniscus profiles fixes the film thickness achieved at $x \to \infty$. The trajectories for Type II solutions, in contrast, are codimension zero intersections of W^∞ and $W^s(T)$. Such trajectories persist under perturbations of the parameters.

The invariant manifolds are approximated by numerically computing individual trajectories, using the LSODE ordinary differential equation solver [21], starting from appropriate initial data and then computing forwards in x for W^∞, or backwards for the stable manifolds of B and T. Specifically, for $W^s(B)$, we choose initial data $(h, v, w) = B \pm \beta \vec{u}_1$, where β is taken to be small, in the range of 10^{-8} to 10^{-3}, and $\vec{u}_1$ is the normalized eigenvector pertaining to the real negative eigenvalue of $J_F(B)$. The matrix $J_F(B)$ denotes the Jacobian of the right hand side of (11) with respect to (h, v, w), evaluated at the equilibrium B. We also remark that normalization is done here with respect to the 2-norm. For the two-dimensional manifold $W^s(T)$ we use $(h, v, w) = T + \beta[\cos(\theta)\vec{u}_2 + \sin(\theta)\vec{u}_3]$ for θ values between 0 and 2π. The vectors $\vec{u}_2$ and $\vec{u}_3$ are either the normalized eigenvectors if the two eigenvalues of $J_F(T)$ are real or, if they are complex conjugate, we use orthonormalizations of the real and imaginary parts of the eigenvectors.

For W^∞ we find approximate initial data by evaluating (15) and its first two derivatives at some sufficiently large cut-off $x = -L$; a typical choice is $L = 20$. That is, we start integrating with

$$h = -\frac{(-L)}{D} - \ln|-L| + \beta,$$

$$v = -\frac{1}{D} - \frac{1}{(-L)} + \beta D^{1/2}, \quad w = \frac{1}{L^2} + \beta D,$$

where $\beta = C_1 \exp(-D^{1/2}L)$ is varied within a range of values in order to trace out W^∞. For all the examples presented below, we found that using β from a range of values smaller than 0.1 was sufficient to trace out

the required portion of W^∞. Increasing L typically decreased the maximum of this range of β. In terms of the alternative variables $\tilde{u} = 1/h$, $\tilde{v} = h_x$ and $\tilde{w} = h_{xx}$, increasing L and decreasing β puts the initial points closer to the equilibrium $(0, -1/D, 0)$, resulting in trajectories that approach the desired manifold more closely. Hence, it also leads to a better approximation of W^∞ in terms of the variables h, v, and w. We compared the results obtained for the original $L = 20$ to those for larger L (and smaller β) and found little difference. Specifically, the curves traced out by the intersection of the trajectories with the Poincaré plane P, defined below in (16), hardly changed. This indicates that the original choice for L already yields sufficiently accurate approximations for $W^\infty \cap P$.

4.3. Results

In this section we describe what solutions of (8)–(10) are possible as D is varied. We first illustrate our approach by investigating the phase space situation for the specific choice of $D = 0.3220$ used in Example 2 of Section 3, before considering other D values. We note here that all numerical values appearing in this paper are given with four digits of accuracy.

4.3.1. $D = 0.3320$

For a special value of $h_B = h_B^*(D) = 0.4002$, a trajectory of W^∞ connects to B, so we have a Type I solution. We use a shooting method to determine h_B^*,

following $W^s(B)$ backward in x, varying h_B for fixed D, until (10) is satisfied. The resulting Type I trajectory is shown in the phase space by a solid line in Fig. 4(a). Also shown are two dashed lines for trajectories of W^∞ that connect to T, i.e., trajectories of two different Type II meniscus solutions. In a close up of a projection of trajectories near the equilibria (Fig. 4(b)) we can identify further Type II trajectories. Shown there are the solid line for the Type I trajectory connecting to B, two distinct dashed lines labeled a and b connecting to T that are the projections of the Type II trajectories from the left figure, and two more (dashed) lines that pass very close near the equilibrium B but then connect to T, hence also representing Type II solutions. These two lines are labeled c and d and are virtually indistinguishable except in the immediate vicinity of B.

We also compute intersections of the invariant manifold with the Poincaré plane

$$P = \{(h, v, w) : h = 2\}. \tag{16}$$

The specific value of h used in (16) is not crucial, and we have explored the use of values other than $h = 2$. Fig. 5(a) shows the Poincaré plane for these values of D and h_B. The point where the one-dimensional manifold $W^s(B)$, or rather, one branch of it, hits the plane is marked by a plus. Since the two other manifolds of interest here, $W^s(T)$ and W^∞, are two-dimensional, their intersections with P are curves, shown in the figure by a solid and a dashed line, respectively. The plus coincides with the dashed line indicating that
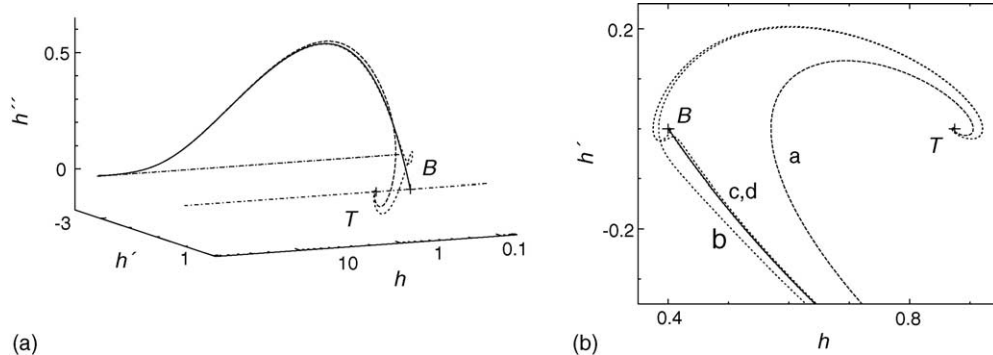

Fig. 4. Two views of trajectories of W^∞ in the (h, h', h'') phase space for $D = 0.3220$ and $h_B = h_B^*(D)$. The left figure (a) is a three-dimensional view; the right figure (b) is a closer view near the stationary points, in a projection onto the h, h' plane. The solid line is a Type I trajectory that connects to B, while the dashed lines go to T, after first approaching B, and represent different Type II solutions. Dash-dotted lines in (a) denote the line $\{(h, -1/D, 0) : h > 0\}$, to which trajectories of W^∞ asymptote for $x \to -\infty$, and the positive part of the h-axis $\{(h, 0, 0) : h > 0\}$. Letters correspond to the labels in Fig. 5.
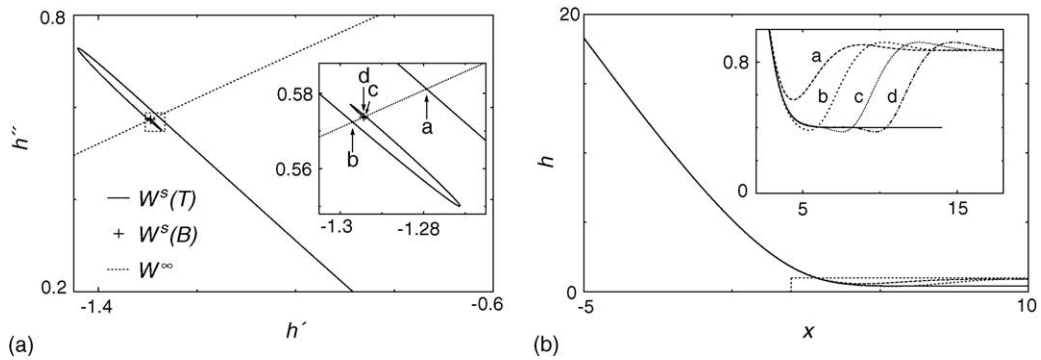
Fig. 5. On the left (a) are shown the intersections of invariant manifolds with the Poincaré plane P defined in the text. The right figure (b) shows the profiles of Type I and Type II solutions corresponding to the intersections of manifolds shown in (a). Insets show the regions in dashed boxes in more detail.

W^∞ intersects $W^s(B)$, i.e., there is a Type I solution. The point where this trajectory passes through P is also the center of an elongated spiral formed by the intersection of $W^s(T)$ with P.

The spiral arises because trajectories from $W^s(T)$ that pass close to the equilibrium B feel the effect of the complex conjugate pair of eigenvalues and are wound into a spiral around the equilibrium. This is similar to a situation previously described for the traveling wave ODE [7,12]. First note there is a heteroclinic orbit that connects the two equilibria, and hence spirals exactly into B. Neighboring orbits approach B but are finally expelled along one of the two branches of $W^s(B)$. Trajectories that are closer to the orbit connecting T to B spend more 'time' in the vicinity of the equilibrium and leave it, after a larger number of windings, along a curve that lies closer to $W^s(B)$. In this way the intersection of these trajectories with P traces out a spiral with an infinite number of windings centered around the point $W^s(B) \cap P$. Since for the special situation $h_B = h_B^*$, the center of the spiral structure $W^s(B)$ coincides with W^∞, there are an infinite number of trajectories in the intersection of $W^s(T)$ and W^∞; each of these intersections corresponds to a different Type II meniscus solution. The first four of these intersections are shown in the Poincaré plane in the inset of Fig. 5(a), labeled by a–d according to the order in which they appear on the spiral.

Profiles of the various meniscus solutions are displayed in Fig. 5(b), with a solid line for the monotonic Type I solution, and other line styles for

the four Type II solutions that correspond to the four intersections in Fig. 5(a) and are labeled accordingly. Note that in contrast to the Type I solution, the Type II solutions are non-monotonic, instead having an oscillatory structure where the meniscus passes over onto the flat film ahead of it. The solution labeled a has the thinnest and shallowest 'dip'. The other solutions b–d each have a minimum that is slightly below h_B within a dip that becomes wider for the higher Type II solutions. Each of these solutions is also shown in Fig. 4(b).

We now change h_B, while still keeping $D = 0.3220$ fixed. For a range of values somewhat larger than h_B^*, the center of the spiral moves to the right of W^∞ (as viewed in P), but there are still multiple trajectories in the intersection of W^∞ and $W^s(T)$. These continue to exist until h_B exceeds a special value $h_B^{(1)} = 0.4304$. Therefore for $h_B^* < h_B < h_B^{(1)}$ there still are multiple Type II solutions, but only a finite, even, number of them. For $h_B > h_B^{(1)}$, the manifolds $W^s(T)$ and W^∞ completely separate, so that no Type II solutions exist in this range. An example of a Poincaré section for this case is shown in Fig. 6(a).

Similarly, for a range of values $h_B^{(2)} \le h_B < h_B^*$, the center of the spiral moves to the left of W^∞ in the Poincaré plane, but remains close enough so that there are multiple Type II trajectories, though there are again only finitely many of them. For h_B below the special value $h_B^{(2)} = 0.3946$, there is only one intersection of $W^s(T)$ and W^∞, visible as a single intersection point in P in Fig. 6(b), so there is now a unique Type II solution.
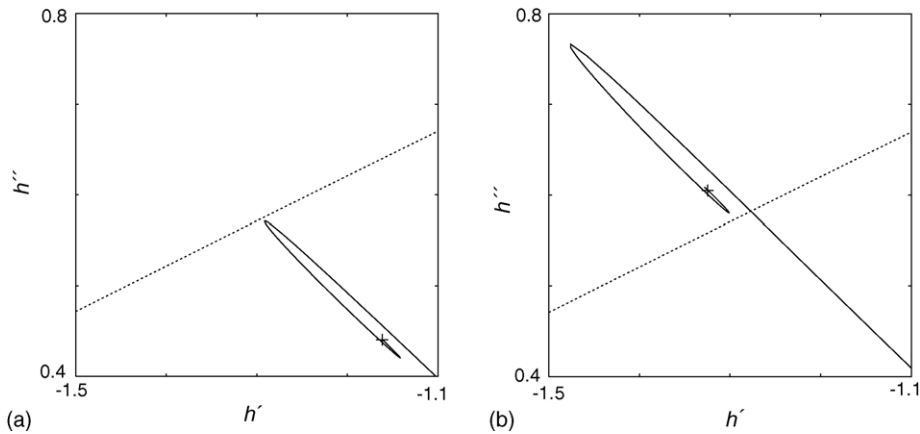
Fig. 6. Poincaré sections for $D = 0.3220$ and different h_B. (a) (left figure) $h_B = 0.4310$ (b) (right figure) $h_B = 0.3930$. Symbols and line styles carry over from Fig. 5(a). In (a) there is no Type II trajectory; in (b) there is exactly one.

4.3.2. Varying D

Changing D for a fixed ϵ means increasing α while decreasing σ_T. As D is increased from zero (for a vertical substrate), it passes two special values, at which the behavior changes from that shown above. As D is varied, the special values h_B^*, $h_B^{(1)}$ and $h_B^{(2)}$ also change. In particular, h_B^* continues to increase monotonically with D until h_B^* reaches 2/3. This happens for a finite value of $D = D_* = 0.8008$. The other critical value is associated with the change of character of the eigenvalues at h_B. This occurs when $\Delta(h_B^*(D); D) = 0$, for $D = D_B = 0.7142$. For $D > D_B$, all eigenvalues of the Jacobian $J_F(B)$ become real and the spiral in $W^s(T) \cap P$ disappears for $h_B = h_B^*(D)$. These critical values divide D into three ranges of interest: $0 < D \leq D_B$, $D_B < D \leq D_*$ and $D > D_*$.

In the first range, $0 < D < D_B$, we obtain the same qualitative picture as for $D = 0.3220$ though the special values h_B^*, $h_B^{(1)}$ and $h_B^{(2)}$ change with D. For each value of D, there is a single Type I meniscus with flat film thickness h_B^*, and a family of Type II meniscii with a range of flat film thicknesses greater than 2/3. The examples in Section 3, which all have D in this range, illustrate the dynamical process by which one of these meniscus solutions is selected. This aspect will be addressed in Section 5.

Turning now to values of D in the second range $D_B \leq D < D_*$, we still find a special value $h_B^*(D)$ for which Type I trajectories exist, which continues to increase monotonically with D until h_B^* reaches 2/3.

For $D = D_B$ and $h_B = h_B^* = 0.6354$, a trajectory from W^∞ connects to the equilibrium B, so that in the corresponding Poincaré section Fig. 7(a), $W^s(B)$ coincides with W^∞. There can only be a finite number of trajectories in the intersection of W^∞ and $W^s(T)$, due to the absence of a spiral in this range of D when $h_B = h_B^*$. In fact, viewed in P the solid line for $W^s(T)$ seems to end at $W^s(B)$ without intersecting the dashed line for W^∞. This leads us to conjecture that when $D_B \leq D < D_*$, there are no Type II meniscus solutions at all, for $h_B = h_B^*(D)$.

For h_B slightly larger than h_B^*, $W^s(B)$ moves to the right of W^∞ in P. In the example shown in Fig. 7(b), we see that $W^s(T) \cap P$ ends right at $W^s(B) \cap P$, without visibly curving around this point, so there is no possibility for an intersection of the manifolds $W^s(T)$ and W^∞, i.e., there are no Type II trajectories. We conjecture that this is true for all h_B in $h_B^*(D) < h_B < 2/3$, when D is in this range.

For h_B smaller than h_B^*, the plus representing $W^s(B)$ in P moves to the left of W^∞, as seen in Fig. 7(c). Since here $\Delta(h_B)$ is positive for small enough h_B, the spiral in $W^s(T)$'s intersection with P reappears, but the rate at which it grows seems to be lower than the rate at which $W^s(B)$ and W^∞ separate. In fact, in Fig. 7(c) the spiral appears to be so small that it is not visible on the scale of the figure. Hence, there is exactly one intersection of $W^s(T)$ and W^∞. We conjecture that for all $0 < h_B < h_B^*(D)$ and $D_B \leq D < D_*$, there is always a unique Type II trajectory.
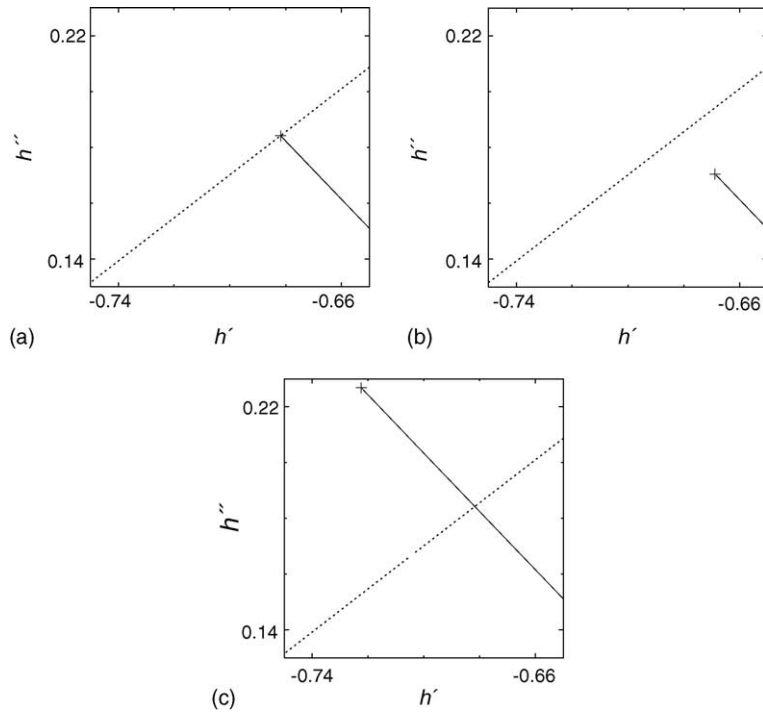
Fig. 7. Poincaré sections for $D = D_B = 0.7142$ and (a) $h_B = h_B^*(D) = 0.6354$ (b) $h_B = 0.6370$ (c) $h_B = 0.6300$. Symbols and line styles carry over from Fig. 5(a).

Finally, we consider the third range, $D > D_*$. For $D = 1$ and all h_B less than $2/3$, the intersections of $W^s(B)$ and W^∞ with the Poincaré plane remain a finite distance apart. The spiral in $W^s(T)$ is absent for a range of h_B near $2/3$, when $W^s(B)$ is closest to W^∞ (in P). We conjecture that for $D > D_*$ and all h_B, there are no Type I solutions, and a unique Type II solution.

5. Summary

Fig. 8 summarizes for which values of D and h_∞ we find a stationary meniscus solution with $h \to h_\infty$ for $x \to \infty$. All solutions that have a far-field thickness below $h_\infty = 2/3$ (dotted horizontal line in the figure) are Type I solutions, while the ones with larger thickness are of Type II.

A single branch of Type I solution exists only for $D < D_*$, so that the thickness h_∞ of the film emerging from the meniscus is necessarily equal to the D-dependent value h_B^*. This value is shown as a solid line in Fig. 8 that tends to $2/3$ when $D = D_*$. For $D \to 0$,
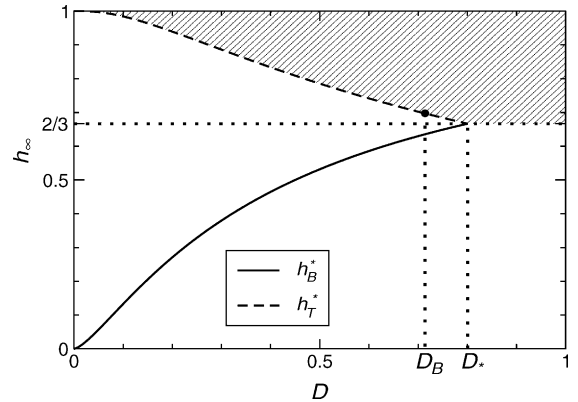

Fig. 8. The occurrence of steady state solutions for different D and far-field film thicknesses h_∞. Type I solutions only exist on the solid line that ends at $(D_*, 2/3)$. For each value of $D < D_*$, the thickness h_∞ is given by h_B^*, determined in Section 4. The complementary value h_T^* is obtained as the upper solution h of $f(h) = f(h_B^*)$. Type II solutions exist for the range of values (D, h_∞) in the gray shaded area, which is delimited from below by $2/3$ for $D \geq D_*$ and by h_T^* for $D < D_*$. In fact, for $D < D_B$, they still exist slightly below h_T^*, down to a value $h_T^{(1)}$; this is not shown in the figure.

the numerical data shows that the film thickness for this branch of solutions tends to zero; in fact, closer inspection in a log-log plot indicates that $h_\infty = h_B^* \sim D^{3/2}$. Note however, that the approximations used in the derivation of (6) are only valid if $D \gg \epsilon$. Indeed, previous results by Carles and Cazabat [2], Fanton et al. [3] and Münch [12] on stationary meniscus solutions of (1) for lower α show that in the limit $\epsilon, D \to 0$, $D \ll \epsilon$, the film thickness behaves like $\epsilon^{3/2}$, i.e. decays more slowly than the result $h_\infty \sim D^{3/2}$ obtained from the lubrication model (6).

On the other hand, these earlier asymptotic approximations of the nonlinear curvature model thickness deteriorate for larger D. A quantitative comparison of the nonlinear curvature model thickness with the leading order solution from [12] (also stated in [2,3]), using a realistic shear stress [19] that yields $\delta = 7.87 \times 10^{-3}$, shows that, except for very small D, the values deviate noticeably. The asymptotic approximation always overestimates the thickness for the nonlinear curvature model. For values larger than about $D = 0.1$ (where, we note, D is about equal to ϵ for the aforementioned choice of δ), the nonlinear curvature model thickness rapidly approaches the solid line in Fig. 8, which remains a good approximation up to $D = D_*$. Carles and Cazabat explain the failure of the basic asymptotic formula by the increasing importance of gravity for larger values of h_∞, and suggest an improved formula that is also used in [19] (where it appears as Eq. (1)). Their new expression indeed provides a better approximation for a larger range of D, but still deteriorates for large D, for which it underestimates the thickness in Fig. 8. In fact, it remains well below 2/3 even for D significantly larger than D_*.

Type II solutions exist in the first range of D, $0 < D < D_B$, for thicknesses $h_\infty \geq h_T^{(1)}$, with multiple solutions arising in a thin strip $h_T^{(1)} < h_\infty \leq h_T^{(2)}$ that contains h_T^*, and merges into h_T^* at the point (D_B, h_T^*) marked by a circle in the figure. Here $h_T^{(1)}$ is defined as the root $h > 2/3$ of $f(h) = f(h_B^{(1)})$, where $h_B^{(1)}$ is the special value introduced in the previous section; the values h_T^* and $h_T^{(2)}$ are defined analogously. Only h_T^* is shown in Fig. 8, as a dashed line. For $D_B \leq D < D_*$, we have the simpler situation of either no Type II solutions if $h_\infty \leq h_T^*$, or exactly one, if $h_\infty > h_T^*$. In the third range of D discussed in this paper, $D > D_*$, we have exactly one Type II solution for all h_∞ above 2/3.

A feature of our results is that for a given $D < D_*$ (i.e., a fixed experiment set-up) there is a gap in accessible coating thicknesses and flow rates. A similar gap has been seen for a film which is dragged out by a moving substrate [15]. On the other hand, we have demonstrated that there are no Type I meniscii for D beyond D_*; estimates based on the Type I thickness are not valid for large D. Hints of the bifurcation seen here are evident in Wilson's results for the drag-out problem [13].

5.1. Interaction of the meniscus solutions with the shock dynamics

A complementary diagram to Fig. 8 that maps out which wave structures arise at the contact line for different values of the parameter D and left states h_∞ (and selected precursor thicknesses b) is given in [8]. Overlapping the two diagrams yields additional information about which dynamics are possible for a thin film emerging from the meniscus, and which type of meniscus solution is established in the long run, for different values of D. An outline of the picture that emerges is given here by discussing the three examples introduced in Section 3; a fuller account that also investigates the stability of the meniscus solutions will be given in an upcoming paper. The issue of meniscus thickness and different meniscus solutions may also have some relevance for the work by Haskett et al. [22], where a Marangoni-driven film is controlled by localized heating with a laser.

For Example 1, the thickness h_B^* of the Type I solution for $D = 0.1021$ is fairly small; it corresponds to label C_1 on the graph of the flux function (Fig. 9). Theory [7,8] predicts that for a class of monotonic initial data connecting b with a left state below a certain threshold, a single compressive wave arises. This threshold, h_{thresh} say, depends on b and D, and can be determined by investigating the phase space for the traveling wave ODE of the lubrication model (6). For the choice of b and D in this example, h_B^* indeed lies below the threshold. So we observe the formation of a single compressive wave and a Type I meniscus solution. The left state of the wave is determined by the unique far-field thickness of the Type I meniscus, i.e., $h_\infty = h_B^*$, which does not depend on b. The speed of the compressive wave is given by the slope of the chord connecting C_1 and P in Fig. 9.
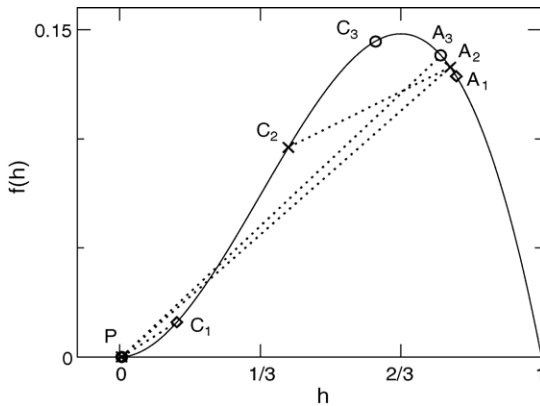
Fig. 9. Situation on the graph of the flux function $f(h) = h^2 - h^3$ for each of the three examples of numerical simulations introduced in Section 3. Boxes, crosses and circles mark the points $(b, f(b))$ (label P), $(h_{uc}, f(h_{uc}))$ (labels A_i) and $(h_B^*, f(h_B^*))$ (labels C_i), with a different symbol for each example $i = 1, 2$ and 3. Dotted lines indicate chords for the shock wave profiles that appear in the simulations.

Raising the value of D to 0.3220 in Example 2 significantly increases h_B^* so that it is now larger than h_{thresh}, which has hardly changed. For this case, formation of a double compressive/undercompressive wave is expected [7,8], with a unique b- and D-dependent left state h_{uc} for the leading undercompressive wave. Its value can again be obtained from the traveling wave ODE. The chords A_2C_2 and A_2P for the two waves have positive slope, indicating that both waves move away from the meniscus, albeit with different speeds. The meniscus converges to a Type I solution which determines $h_\infty = h_B^*$, as in the previous example.

Example 3 uses an even larger value of D. Now h_B^* is not only above h_{thresh}, but is so large that the chord A_3C_3 for the trailing Lax wave would have a negative slope, and therefore would move backwards! Therefore, no Lax wave is able to separate from the meniscus. However, an undercompressive wave still appears, and this has a positive speed. The meniscus settles into a Type II solution with a far-field that is determined by the undercompressive height $h_{uc} > 2/3$.

Interestingly, a structure resembling a stationary Lax wave at the meniscus was reported by Schneemilch and Cazabat [19] for experiments at a large inclination angle of $\alpha = 70°$. This would seem to correspond to the oscillation seen in our Type II meniscus profiles.

References

[1] A.M. Cazabat, F. Heslot, S.M. Troian, P. Carles, Finger instability of thin spreading films driven by temperature gradients, Nature 346 (6287) (1990) 824–826.
[2] P. Carles, A.-M. Cazabat, The thickness of surface-tension-gradient-driven spreading films, J. Colloid Interface Sci. 157 (1993) 196–201.
[3] X. Fanton, A.-M. Cazabat, D. Quéré, Thickness and shape of films driven by a Marangoni flow, Langmuir 12 (24) (1996) 5875–5880.
[4] D.E. Kataoka, S.M. Troian, A theoretical study of instabilities at the advancing front of thermally driven coating films, J. Colloid Interface Sci. 192 (1997) 350–362.
[5] D.E. Kataoka, S.M. Troian, Stabilizing the advancing front of thermally driven climbing films, J. Colloid Interface Sci. 203 (1998) 335–344.
[6] A.L. Bertozzi, A. Münch, X. Fanton, A.-M. Cazabat, Contact line stability and 'undercompressive shocks' in driven thin film flow, Phys. Rev. Lett. 81 (23) (1998) 5169–5172.
[7] A.L. Bertozzi, A. Münch, M. Shearer, Undercompressive waves in driven thin film flow, Physica D 134 (1999) 431–464.
[8] A. Münch, Shock transitions in Marangoni-gravity driven thin film flow, Nonlinearity 13 (2000) 731–746.
[9] A. Münch, A.L. Bertozzi, Rarefaction-undercompressive fronts in driven films, Phys. Fluids 11 (1) (1999) 2812–2814.
[10] L. Landau, B. Levich, Dragging of a liquid by a moving plate, Acta Physicochim. URSS 17 (1942) 42–54.
[11] L.W. Schwartz, On the asymptotic analysis of surface-stress-driven thin-layer flow, J. Eng. Math. 39 (2001) 171–188.
[12] A. Münch, The thickness of a Marangoni-driven thin liquid film emerging from a meniscus, SIAM J. Appl. Math. 62 (6) (2002) 2045–2063.
[13] S.D.R. Wilson, The drag-out problem in film coating theory, J. Eng. Math. 16 (3) (1982) 209–221.
[14] L.M. Hocking, Meniscus draw-up and draining, Eur. J. Appl. Math. 12 (2001) 195–208.
[15] H.S. Kheshgi, S.F. Kistler, L.E. Scriven, Rising and falling film flows: viewed from a first-order approximation, Chem. Eng. Sci. 47 (1992) 683–694.

[16] A. Münch, Pinch-off transition in Marangoni-driven thin films, Phys. Rev. Lett. 91 (1) (2003) id: 016105.

[17] V. Ludviksson, E.N. Lightfoot, The dynamics of thin liquid films in the presence of surface-tension gradients, Am. Inst. Chem. Eng. J. 17 (5) (1971) 1166–1173.

[18] M. Schneemilch, A.M. Cazabat, Wetting films in thermal gradients, Langmuir 16 (2000) 8796–8801.

[19] M. Schneemilch, A.M. Cazabat, Shock separation in wetting films driven by thermal gradients, Langmuir 16 (2000) 9850–9856.

[20] A. Münch, B.A. Wagner, Numerical and asymptotic results on the linear stability of a thin film spreading down a slope of small inclination, Eur. J. Appl. Math. 10 (1999) 297–318.

[21] A.C. Hindmarsh, ODEPACK, a systematized collection of ODE solvers, in: R.S. Stepleman et al. (eds.), Scientific Computing, Vol. 1 of IMACS Transactions on Scientific Computation, North-Holland, Amsterdam, 1983, pp. 55–64.

[22] R. P. Haskett, T. P. Witelski, J. Sur, Localized Marangoni forcing in driven thin films, Physica D 209 (2005) 117–134.